Supplementary Materials for

Medium-density amorphous ice

Alexander Rosu-Finsen, Michael B. Davies, Alfred Amon, Han Wu, Andrea Sella, Angelos Michaelides*, Christoph G. Salzmann*

Correspondence to: c.salzmann@ucl.ac.uk, am452@cam.ac.uk

This PDF file includes:

Other Supplementary Materials for this manuscript include the following:

Materials and Methods

1. Low-temperature ball milling

Medium-density amorphous ice (MDA) was prepared using a liquid-nitrogen cooled CryoMill from Retsch. A 35 mL steel grinding jar was cooled with external liquid nitrogen. Eight milliliters of Milli-Q water were added and the resulting ice was coarsely ground with a pestle. Eight pre-cooled 10 mm-diameter stainless steel balls were then added, the grinding jar was closed tightly and mounted on the pre-cooled CryoMill. The ice was then subjected to up to 80 milling cycles. Each milling cycle included shaking the jar at 5 s^{-1} for 7.5 minutes followed by more vigorous shaking at 20 s^{-1} for 5 minutes. The aim of the lower-frequency shaking was to distribute the material well within the grinding jars before the more intense shaking regimes. After the ball milling, the grinding jar was quickly transferred into a liquid-nitrogen bath and the ball-milled ice was recovered from the grinding jar under liquid nitrogen for further analysis (see Movie S1).

Ice I*h* ball-milling experiments with 40 milling cycles were also carried out using different ball materials including eight 10 mm-diameter Teflon-coated or hardened-steel balls from Retsch.

In addition to using ice I*h* as a starting material, ball-milling experiment were performed using 8 g of dry NH_4F (Sigma Aldrich) as well as the ice II, ice IX and ice V high-pressure phases. These experiments were conducted with 40 milling cycles and eight 10 mm-diameter stainless-steel balls.

The high-pressure phases of ice were prepared using a piston-cylinder setup in combination with a Z100 Zwick Test Machine (Zwick/Roell Group, Germany) as described in detail in ref. (*45*). The high-pressure experiments were carried out with a 13-mm diameter pressure die. Indium cups were inserted into the bore of the die and the assembly was cooled with liquid nitrogen before injecting 1.0 mL of Milli-Q water. The pressure was then increased at 5 kN min^{-1} to the target pressure for making the high-pressure phase of ice followed by isobaric heating to the target temperature after which the samples were quenched with external liquid nitrogen, the pressure released and the ice samples recovered under liquid nitrogen. The target pressures and temperatures were 0.3 GPa / 244 K, 0.3 GPa / 254 K and 0.5 GPa / 250 K for preparing ices II, IX and V, respectively. In order to obtain the 8 g required for the ball-milling experiments, eight samples of each high-pressure phase of ice were prepared. These were freed from the indium and combined in a grinding jar for ball milling.

2. Optical imaging of the ball-milled ice samples

A dilute suspension of ball-milled ice in liquid nitrogen after 80 milling cycles was poured onto the copper substrate of a precooled Oxford Instruments Microstat^N cryostat followed by quick evacuation of the cryostat. Optical images of ball-milled ice particles were then obtained at 80 K using a Keyence VHX-970F digital microscope with a 100-fold magnification objective.

3. Density measurements of ice samples in liquid nitrogen at 77 K

Using the Archimedean buoyancy principle, the densities of MDA and other ice samples were determined in liquid nitrogen using a balance with an accuracy of ±0.1 mg. A cup (10 mm diameter, 15 mm high and ~0.45 g) was fashioned out of aluminum foil and hung on a tantalum wire from the weighing hook on the underside of the balance. A Dewar filled with liquid nitrogen was then moved towards the cup, and the weight of the cup was noted with the cup above and submerged in the liquid nitrogen (LN2). Ice samples were then transferred into the cup under liquid nitrogen and the weight was noted while ensuring that there was no ice

formation on the wire. The filled cup was then raised just above the liquid nitrogen level and the weight was noted as soon as the liquid nitrogen inside the cup had evaporated. The weight of the sample in the gas phase, $m_{\text{in N2 gas}}$, and in the liquid, $m_{\text{in LN2}}$, was then calculated by subtracting the corresponding values of the empty cup recorded earlier. The density of the ice sample, ρ, can then be calculated using equation 1 which takes the buoyancy of the sample in the liquid and the gas phase into account.(*46*)

$$\rho = \frac{m_{in\ N_2\ gas}}{m_{in\ N_2\ gas} - m_{in\ LN_2}} \times \left(\rho_{LN_2} - \rho_{N_2\ gas}\right) + \rho_{N_2\ gas} \quad (1)$$

The densities of liquid nitrogen at the boiling point, ρ_{LN2}, and gaseous nitrogen at 78 K, ρ_{N2} gas, are 0.808 g cm^{-3} and 0.005 g cm^{-3}, respectively.

To test the method, crystalline ice samples of known densities were measured. For ice I*h* and ice II, densities of 0.90 ± 0.02 and 1.15 ± 0.08 g cm^{-3} were obtained which compares well with the expected crystallographic densities from the literature of 0.92 and 1.17 g cm^{-3}, respectively.(*47*, *48*) The densities of the ball-milled samples as a function of the ball-milling cycles are shown in Fig. 1E. The values lie in the density range between ice I*h* and ice II for which the validity of our method has been established.

To ensure that the potentially high surface area of the ball-milled ice and associated microporosity does not affect the density measurements, amorphous solid water (ASW) was prepared by physical vapor deposition of H_2O onto a 77 K copper substrate. ASW is well known to have a high surface area with associated microporosity.(*49*) The procedure for preparing ASW in our lab is described in detail in ref. (*50*). The density of ASW was determined as 0.94 ± 0.02 g cm^{-3} with our method which agrees very well with reported literature values.(*51*) Any formation of nitrogen gas inside micropores would lead to a decrease of the measured density which goes against the trend of increasing density of ball-milled samples compared to ice I*h*.

4. Low-temperature compression experiments

MDA samples were transferred into indium gaskets located inside 8 mm-diameter harden-steel piston cylinders precooled with liquid nitrogen. Compression at 77 K for a range of pressures up to 1.6 GPa was performed at 5 kN min^{-1} using the computerized Zwick Roell Proline Z100TN Universal Testing Machine. Following decompression, the samples were recovered under liquid nitrogen for further analysis. In one experiment, a compressed sample was heated to 250 K at ambient pressure to transform the sample to ice I*h* and then compressed again to 1.6 GPa at 77 K. In another experiment, MDA was heated isobarically to 145 K at 0.25 GPa, quenched and also recovered under liquid nitrogen.

5. Differential Scanning Calorimetry (DSC)

Stainless-steel pans were filled with ice samples under liquid nitrogen and transferred into a pre-cooled PerkinElmer DSC 8000 advanced double-furnace differential scanning calorimeter. The samples were heated from 95 to 260 K at 10 K min^{-1} and transformed to ice I*h*. A second scan from 95 to 260 K was then recorded and used as a background for the first scan. Finally, the amounts of H_2O in the DSC pan were determined by recording the endothermic melting at 0°C and using 6012 J mol^{-1} as the enthalpy of melting.

As shown for LDA,(*52*) annealing at temperatures below the crystallization temperature can yield endothermic steps in the heat capacity which is the calorimetric signature for a glass

transition. MDA samples were annealed for 6 hours at 105, 110, 115, 120 and 130 K, and DSC scans were recorded at 10 K min^{-1}. No endothermic steps and therefore no glass transitions could be detected in any of the DSC scans (Fig. S21).

6. Optimization of the low-temperature ball-milling conditions

The effect of the diameter and number of steel balls on the formation of MDA through ball milling was investigated. Following the recommendations of the manufacturer of the cryomill (Retsch) eight 10 mm, three 15 mm and one 20 mm diameter steel ball(s) were used for a range of experiments with a 35 mL grinding jar and 8 g of ice I*h*. As discussed in the main article and shown in Fig. 1D, the area of the exotherm at ~150 K recorded with differential scanning calorimetry (DSC) indicates the progress of the ball milling process. Apart from small deviations for three ball-milling cycles, the areas of the exotherms are independent within error of the diameter of the steel balls for ball-milling cycles up to 24 as shown in Fig. S5. Stainless-steel balls give the best results in term of the amorphous content compared to Teflon-coated or hardened steel balls (Fig. S6).

7. Preparation of other types of amorphous ice for comparison

HDA was prepared by compression of ice I*h* to 1.6 GPa at 77 K and 5 kN min^{-1}.(*53*) To make vHDA, HDA was decompressed to 1.1 GPa at 5 kN min^{-1} and heated to 165 K.(*54*) After this, the vHDA was quenched with liquid nitrogen and recovered at ambient pressure under liquid nitrogen. A sample of eHDA was made by decompressing HDA from 1.6 GPa to 0.25 GPa at 5 kN min^{-1} followed by heating to 145 K and the sample was also recovered at ambient pressure.(*55*) LDA was obtained by heating HDA to 125 K at ambient pressure.(*53*)

8. X-ray diffraction measurements

Ice and NH_4F samples were transferred into a purpose-built sample holder with Kapton windows under liquid nitrogen. Powder X-ray diffraction patterns were then recorded by mounting the sample holders on a Stoe Stadi P diffractometer with Ge 111 monochromated Cu Kα1 radiation at 40 kV and 30 mA, and a Mythen 1K area detector. The temperature of the samples was controlled with an Oxford Instruments Cryojet HT.

8.1. Quantification of the stacking disorder in ice I*sd* obtained from heating MDA

As shown in Fig. 1C, upon heating MDA at ambient pressure a phase transition to stacking disordered ice I (ice I*sd*) is observed. Fig. S4A shows the X-ray diffraction patterns of ice I*sd* obtained from MDA and its transition to the stable ice I*h* upon heating. The cubicities, *i.e.* the percentages of cubic stacking, obtained from fitting the diffraction patterns with MCDIFFaX(*56, 57*) are shown as a function of temperature in Fig. S4B.

8.2. Determination of the amorphous fraction in ball-milled samples from X-ray diffraction

From X-ray diffraction data collected upon heating at ambient pressure, such as shown in Fig. 1C, Fig. S6 and Fig. S7, the amorphous fractions of the ball-milled samples were estimated. Upon heating from 95 to 240 K, the amorphous samples containing some ice I*h* transformed to pure ice I*h* which was seen as increases of the Bragg peaks characteristics of ice I*h*. For this analysis, the three most intense low-angle Bragg peaks were used and the ratio of the average peak intensities before and after heating was calculated (Fig. S7). This quantity, F_c, reflects the fraction of ice I*h* present in the original sample. The amorphous fraction, F_a, is then obtained from $1 - F_c$.

9. Raman spectroscopy

Raman spectra were recorded at 80 K using a Renishaw Ramascope (632.8 nm) and an Oxford Instruments Microstat^{N} cryostat.

10. Small-angle X-ray scattering (SAXS)

Ball-milled ice samples were transferred into a self-built aluminum sample holder under liquid nitrogen. The sample holder consists of two 150 × 100 × 20 mm aluminum plates with a 4 mm-diameter bore in the center. One plate contains a 10 mm wide and 1.8 mm deep cylindrical recess with the bore in the middle which was covered with 0.025 mm thick Kapton foil and filled with the ice sample. The second plate with Kapton foil covering the bore and a conical exit at the back was placed on top of the ice sample creating a closed 1.8 mm deep sample environment. The two plates were firmly held together by four M6 screws at the corners. A hollow 3D-printed base made from PLA was attached to the bottom of the two aluminum plates and a Pt100 temperature sensor was firmly inserted through a hole from the side of the aluminum block, close to the sample compartment, and secured with heat-conducting paste. The entire assembly was transferred quickly from liquid nitrogen into the vacuum chamber of a Ganesha 300XL SAXS instrument. After connecting the temperature sensor to a Lakeshore 331 cryogenic temperature controller, the vacuum chamber was evacuated to a base pressure of ~1×10^{-2} mbar within a few minutes. A microfocus X-ray beam was generated with a copper source with a motorized collimation system of 2 sets of 4-blade single crystal slits. SAXS data was collected with a solid-state photon-counting detector (PILATUS 300 K, Dectris AG, Switzerland) mounted on a 1.4 m transverse rail along the beamline. SAXS data in the 0.15 to 0.7 Å^{-1} *Q*-range with a resolution of 0.00179 Å^{-1} was continuously collected every 3 minutes from 80 to 220 K over the course of about 10 hours. The measurements were repeated with an empty sample compartment but including the Kapton foils for background subtractions.

11. Computational simulations

11.1. Preparation of MDA structures

Computationally, MDA was produced in analogy to the experiment by repeatedly shearing an ice I*h* structure. Specifically, a periodic simulation box containing 2,880 TIP4P/Ice(*58*) water molecules at a density of 0.92 g cm^{-3} with hydrogen disorder was constructed using the GenIce software.(*59*) Periodic boundaries are used to approximate an infinitely large structure. Layers of molecules were sheared randomly in terms of the orientation of the shear plane, layer thickness, and magnitude and direction of the displacement. Following each shearing step, geometry optimizations were performed. These steps were repeated, as illustrated in Fig. 2A and Fig. S13, until the calculated X-ray structure factors converged. Common python libraries, as well as the Atomic Simulation Environment package, were used to create the shears.(*60*) The code along with the computational data associated with the paper is publicly available at doi:10.17863/CAM.78718.

Possible layers for shearing were detected by taking histograms of the number density, ρ, of water molecules in *x*, *y* and *z*, and the locations of troughs in ρ were used to define the layers. A randomly selected shear plane (*xy*, *yz*, or *xz*), layer thickness, and displacement vector (magnitude and direction within the plane) were used for each shearing event. Water molecules were kept intact during the shearing processes. The steepest descent algorithm was used for the geometry optimizations with four stopping criteria: an energy quotient (change divided by total magnitude) less than 2.3 – 16, a global force vector magnitude less than 1.0 – 15 kcal mol^{-1}, a maximum of 200,000 iterations, or a maximum of 200,000 force evaluations. The optimization

was terminated upon meeting a single criterion. If the geometry optimization following a particular shear failed to converge (e.g. 'exploding' potential energy) then the shear was undone and a new random shear attempted.

An ice I*h* structure containing 2,880 molecules was deemed to have fully amorphized once its structure factor had converged as shown in Fig. S14. After 10 shears, some of the diffraction characteristics of ice I*h* were still visible. After about 50 shears, the structure factor had converged. Based on this finding, MDA configurations were taken with an additional 'safety margin' after 100 shears for this system size.

Molecular dynamics simulations were performed using the large-scale atomic / molecular massively parallel simulations software (LAMMPS).(*61*) All simulations sampled the NPT ensemble with a timestep of 2 fs. A 10-fold Nosé-Hoover thermostat and anisotropic barostat controlled the temperature and pressure, with relaxation times of 200 fs and 2 ps respectively. For simulations of liquid water an isotropic barostat was employed. Results for each system were taken from production runs of 2 ns. Structure factors and ring statistics were averaged over 40 configurations spaced 50 ps apart, radial distribution functions were taken over 4,000 configurations spaced 0.5 ps apart. MDA, ice I*h* and LDA were sampled at 125 K and 0 atm, whilst liquid water was sampled at 270 K and 0 atm. Initial configurations of LDA were achieved by annealing sheared ice structures at 220 K and 0 atm, and were subsequently cooled to 125 K. System sizes of 2,800 water molecules were used for MDA, ice I*h* and LDA whilst 2,132 water molecules were used for liquid water.

Multiple techniques were used to analyze the structural properties of our systems. X-ray structure factors were calculated using the Debyer software with a cut-off of half the minimum box dimension, and the sinc-function to dampen the cut-off and reduce the Fourier termination effects. Ring statistics were calculated with the Rigorous Investigation of Networks Generated using Simulations (RINGS) software(*62*) and the primitive rings criterion.

The preparation of MDA structures was also attempted via two alternative techniques to shearing: modelling polycrystalline ice structures and an attempt to simulate nano-scale ball bearings propagating through ice. Both proved to be unsuccessful in producing MDA.

11.2. Determining the density of computational MDA at finite temperature

After producing configurations of MDA at 0 K, their structural properties at finite temperatures were obtained by simulating in the NPT ensemble at 125 K and 0 Pa. Systems were first equilibrated for 2 ns, and production runs were then taken across a further 2 ns of simulation.

The density of MDA was determined by taking the mean density during the production run over simulations of five separate MDA initial configurations as shown in Fig. S19. The density of MDA is reported as the mean of the mean values obtained for each simulation, with the error being the standard deviation, giving 0.970 ± 0.002 g cm^{-3}.

11.3. Dependence of the real-space structure on the number of shears

In line with the changes in the structure factor, the oxygen-oxygen pair distribution function and ring statistics are expected to change as a function of the number of shears applied to the initial ice I*h* structure. This dependence is shown in Fig. S15. As observed for the X-ray structure factor both quantities converged after about 50 shears.

11.4. Investigation of the effects of the route taken during the random shearing processes

The iterative shearing process is stochastic in nature. Therefore, it is possible in principle that the final structural properties of MDA could depend on the route taken during the shearing processes. This is explored in Fig. S16 where it is shown that all structural properties of interest are independent of the route taken.

11.5. Investigation into finite-size effects

All results of computational MDA reported in the main manuscript, and other sections of the Supplementary Materials, were obtained from a 2880 water molecule system of ice I*h*, with density of 0.92 g cm^{-3}, in a periodic box of dimensions 46.91 Å, 45.11 Å, 44.12 Å in *x, y* and *z*. The possibility of finite-size effects is explored in Fig. S17 by comparing the structural properties of the MDA configurations at 0 K obtained upon shearing periodic ice I*h* structures containing 1600, 2880, 4704 and 10368 water molecules.

The level of amorphization in a system will approximately depend on the number of shears per unit volume. Hence, in each case, values are reported for a shear-number density of 1.071 nm^{-3} (within ± one shear) which is the same shear density as achieved from applying 100 shears to the 2880 water molecule system.

All structural properties are unaffected by increasing the system size to at least the level of interest of the current study. Thus, finite size effects appear to not play a role in the results reported (Fig. S17).

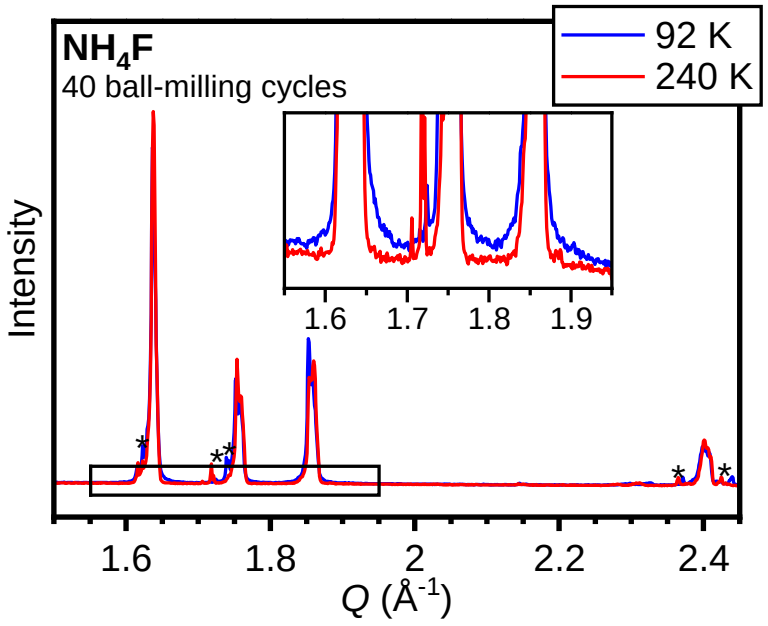

Fig. S1.

Effect of cryogenic ball milling on the diffraction pattern of NH_4F I*h*. X-ray diffraction data (Cu Kα) of NH_4F I*h* after 40 low-temperature ball-milling cycles (92 K) and after heating to 240 K. NH_4F I*h* is isostructural with ice I*h*. The broadening of the Bragg peaks as a consequence of the ball milling can be seen in the inset. Small peaks highlighted by asterisks are due to small NH_4F particles on the outside of the sample holder.

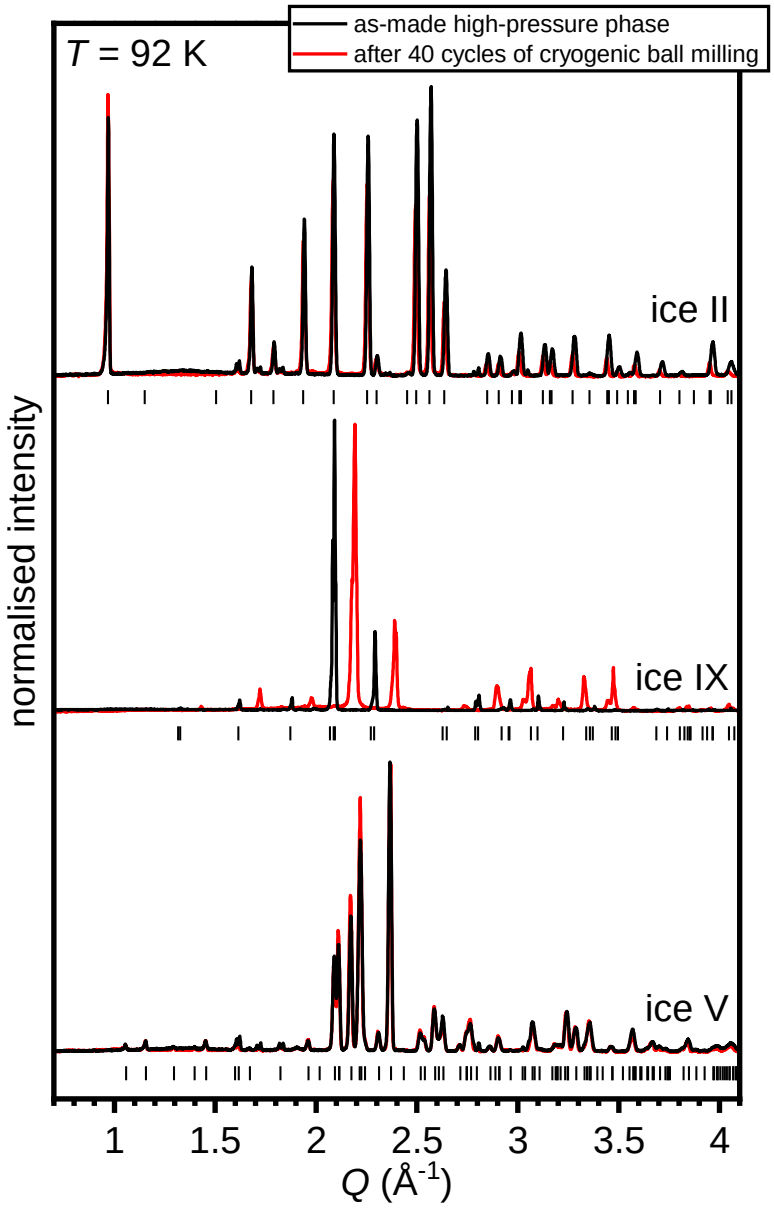

Fig. S2.

X-ray diffraction patterns of the ice II, IX and V high-pressure phases of ice before and after cryogenic ball milling. Tick marks indicate the expected positions of the Bragg peaks. Variations in the intensities of the Bragg peaks, most clearly visible for the ice IX samples, are due to preferred orientations of the crystals during measurement. No amorphous features can be observed for any of the ball-milled samples.

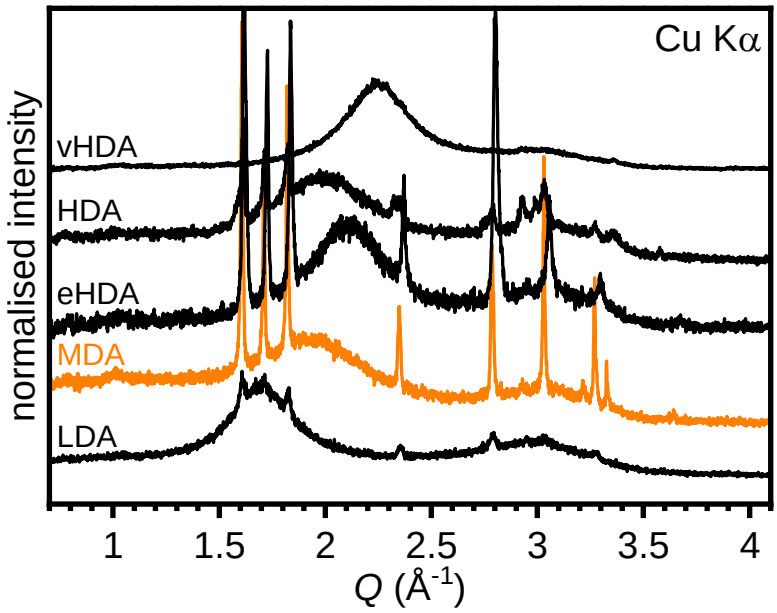

Fig. S3.

Comparison of the X-ray diffraction patterns (Cu Kα) of the amorphous ices at 90 K and ambient pressure. The tickmarks indicate the positions of the Bragg peaks of ice I*h* which is present in some of the amorphous ices either from vapor condensation during the sample transfer or as an impurity. The dashed vertical lines indicate the peak positions of MDA.

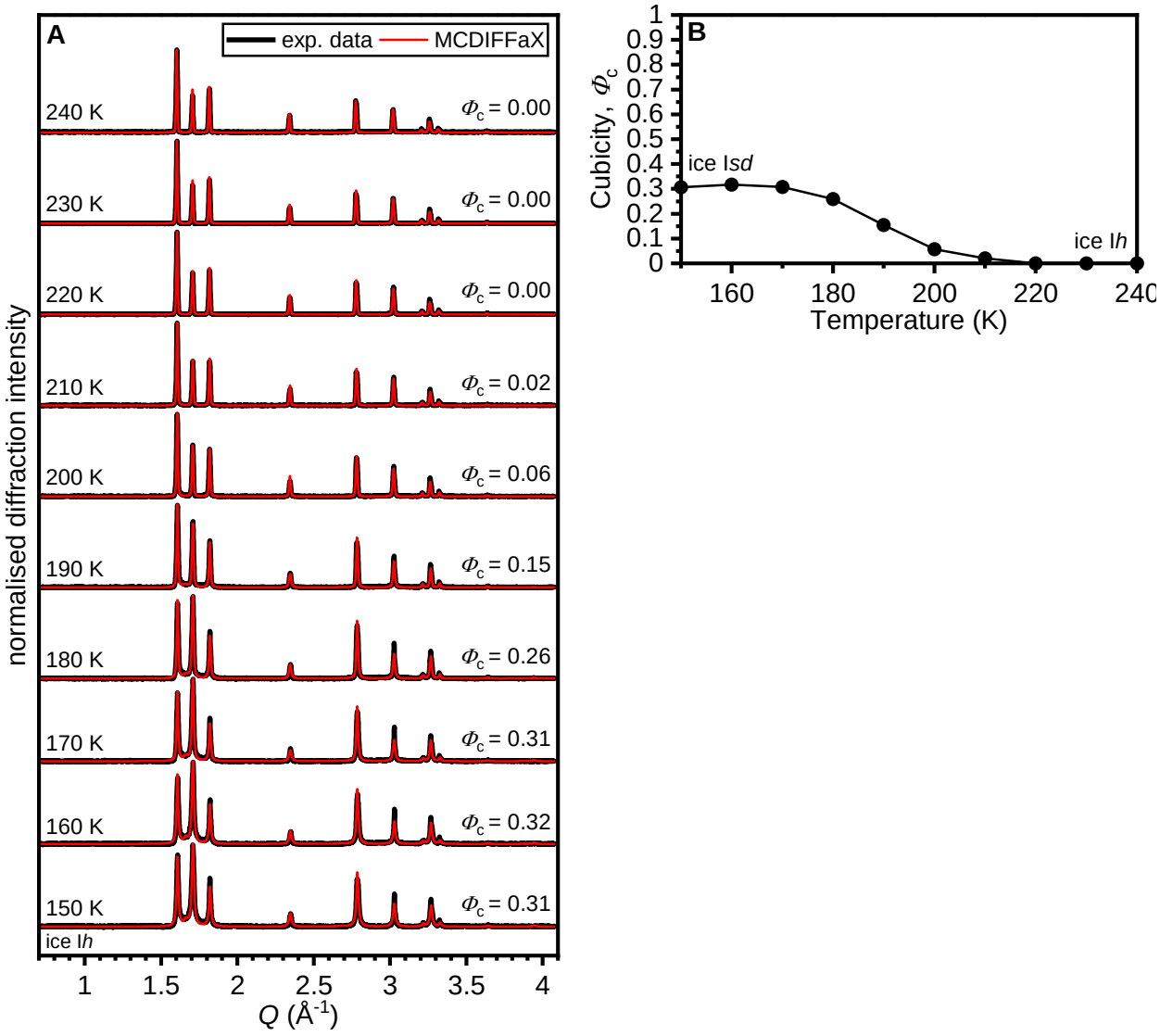

Fig. S4.

Analysis of the stacking disorder after recrystallizing MDA. (A) X-ray diffraction patterns recorded upon heating ice I*sd* obtained from MDA at ambient pressure. The experimental data is shown as black lines and the MCDIFFaX(*56, 57*) fits in red. Tick marks at the bottom indicate the positions of the Bragg peaks of ice I*h*. (B) Cubicities of ice I*sd* as a function of temperature.

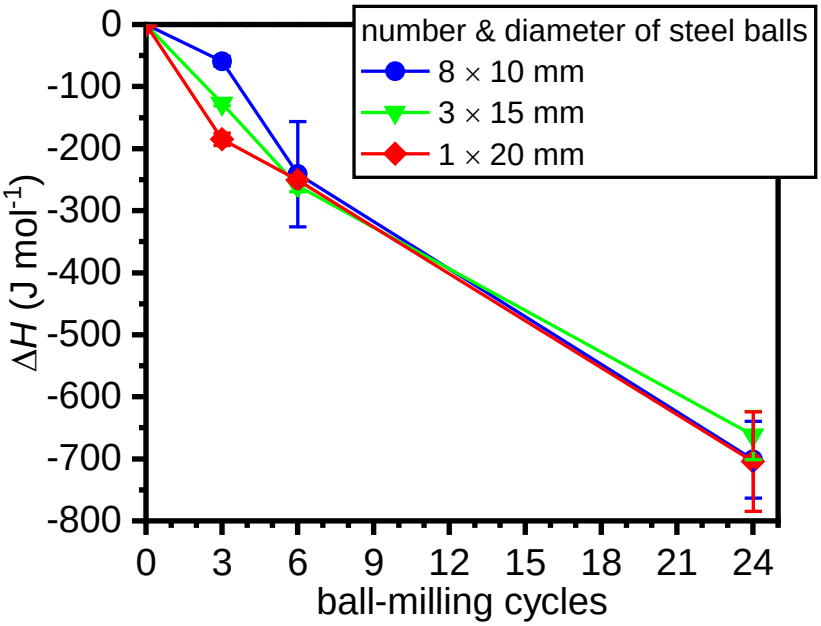

Fig. S5.

Effects of number and diameter of the stainless-steel balls used for cryogenic ball milling on the recrystallization exotherm of MDA. Enthalpies of the exotherms at ~150 K recorded with DSC upon heating ball-milled samples using different numbers and diameters of steel balls at 10 K min^{-1}.

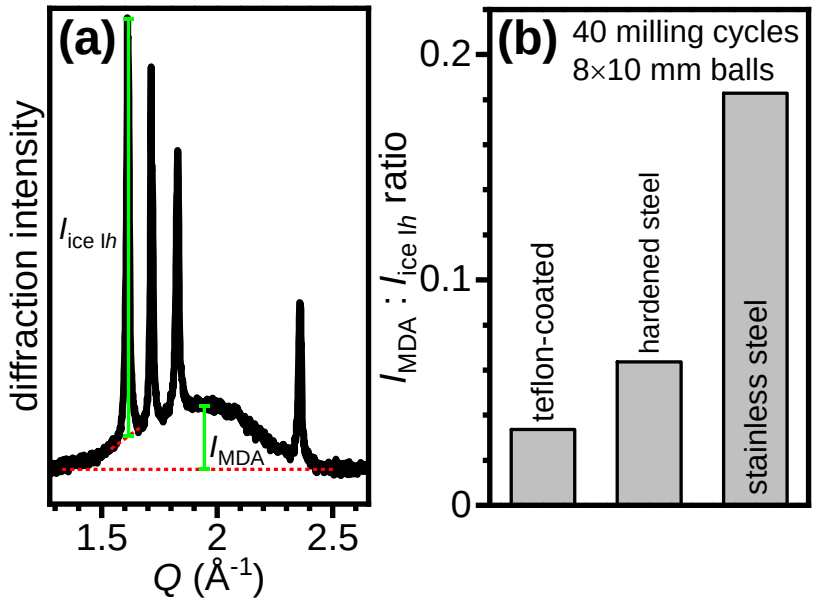

Fig. S6.

Effect of different ball materials on the formation of MDA. (a) Illustration of the analysis of the peak intensities of the MDA and ice I*h* components in the X-ray diffraction patterns. (b) Peak-intensity ratios of ice I*h* ball-milled for 40 cycles with eight 10-mm diameter balls consisting of Teflon-coated, hardened or stainless steel. The highest peak intensity ratio and hence the most complete conversion to MDA was observed for stainless-steel balls.

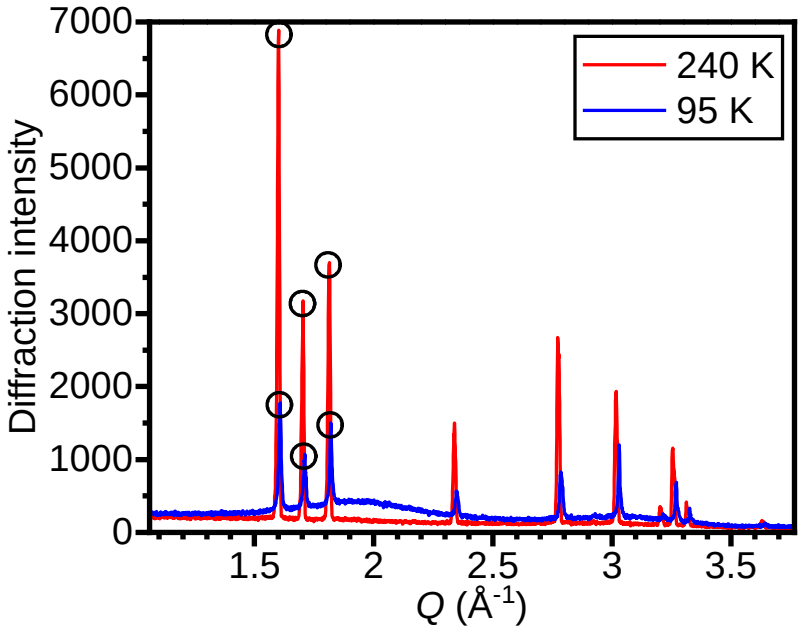

Fig. S7.

X-ray diffraction data (Cu Kα) used for the determination of the amorphous fraction. The balled-milled sample after 80 milling cycles at 95 K was heated to 240 K to achieve the full conversion to ice I*h*. The Bragg peaks used for the quantitative analysis of the amorphous fraction in the ball-milled sample are highlighted with open circles.

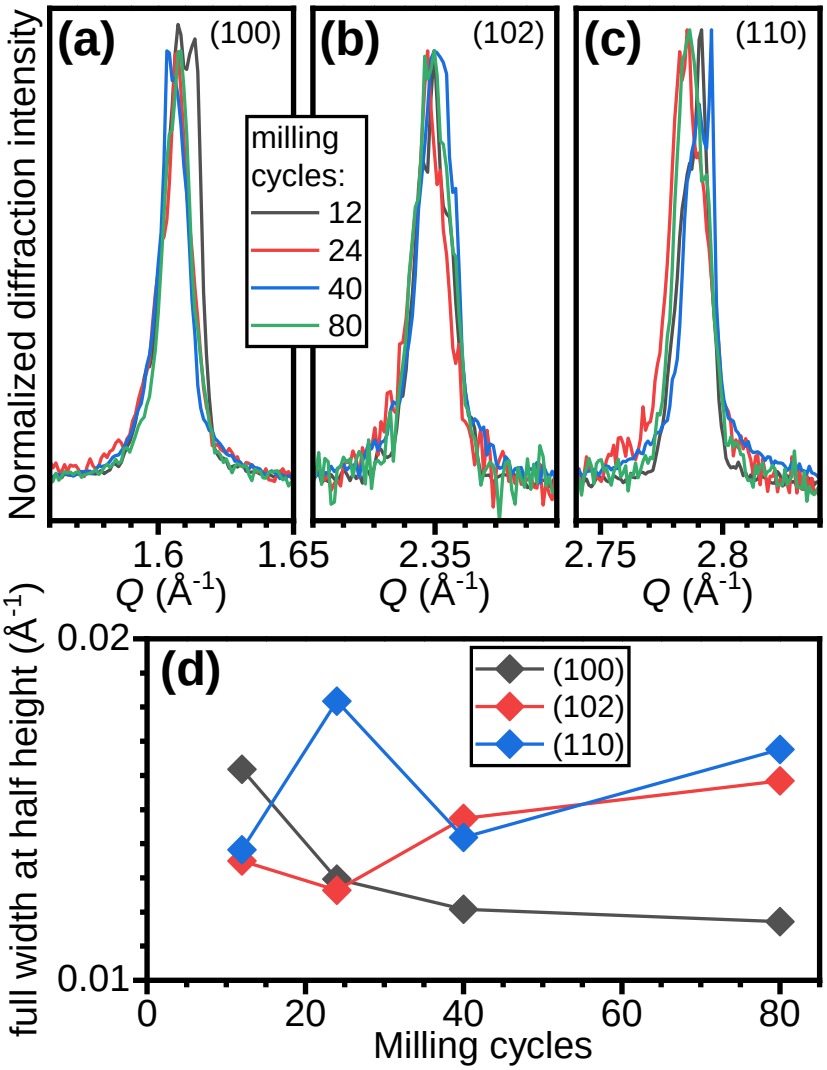

Fig. S8.

Absence of systematic Bragg-peak broadening of the ice I*h* contaminant in ball-milled ice samples. (a-c) (100), (102) and (110) Bragg peaks of the ice I*h* contaminants after 12, 24, 40 and 80 ball-milling cycles. For each peak, the background and contributions from MDA were subtracted and the peak intensities normalized. (d) Full width at half height of the Bragg peaks shown in (a-c) as a function of the milling cycles.

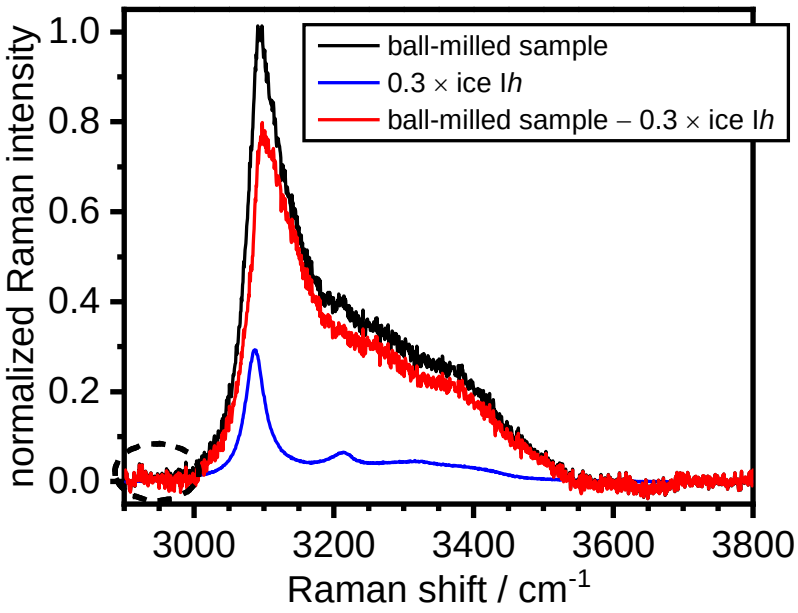

Fig. S9.

Subtraction of an ice I*h* component from the Raman spectrum of a ball-milled sample for 80 cycles. A maximal contribution of 30% ice I*h* can be subtracted before the resulting spectrum shows an unphysical negative slope in the highlighted region below 3000 cm^{-1}. The spectrum of the ball-milled sample is shown in black, the 30% contribution of ice I*h* in blue and the resulting spectrum after subtraction in red.

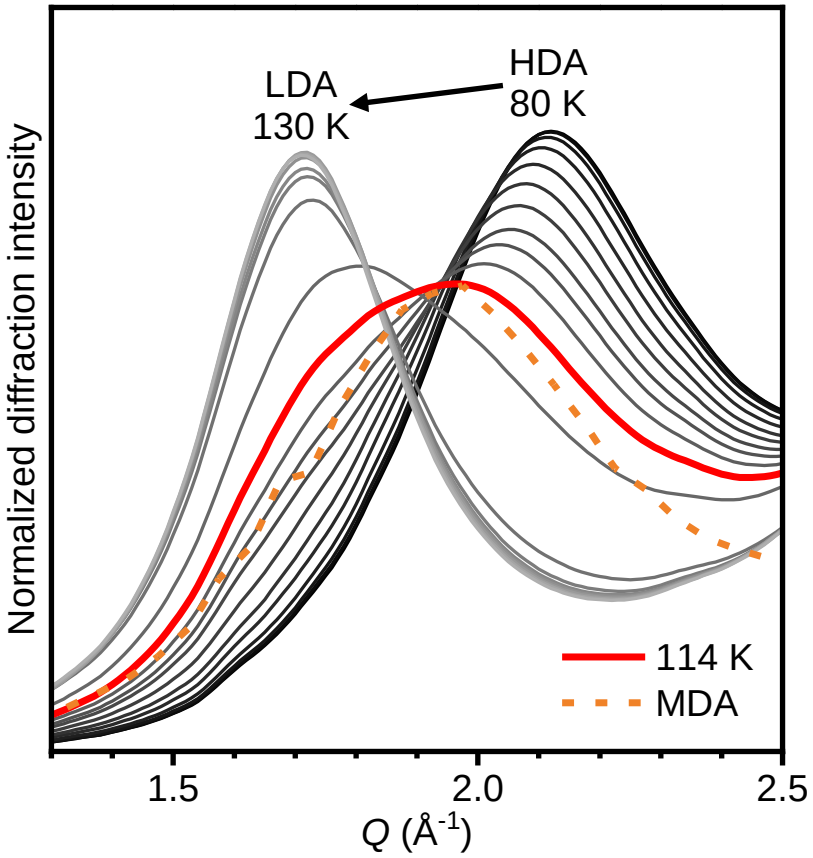

Fig. S10.

Comparison of the first strong diffraction peak (FSDP) of MDA with the transition states during the HDA to LDA phase transition upon heating from 80 to 130 K from ref. (*63*). The best agreement in terms of peak position is found for the 114 K data highlighted in red. Yet, the diffraction feature of the HDA to LDA transition state at 114 K is asymmetric and broader compared to the MDA feature (orange dashed line).

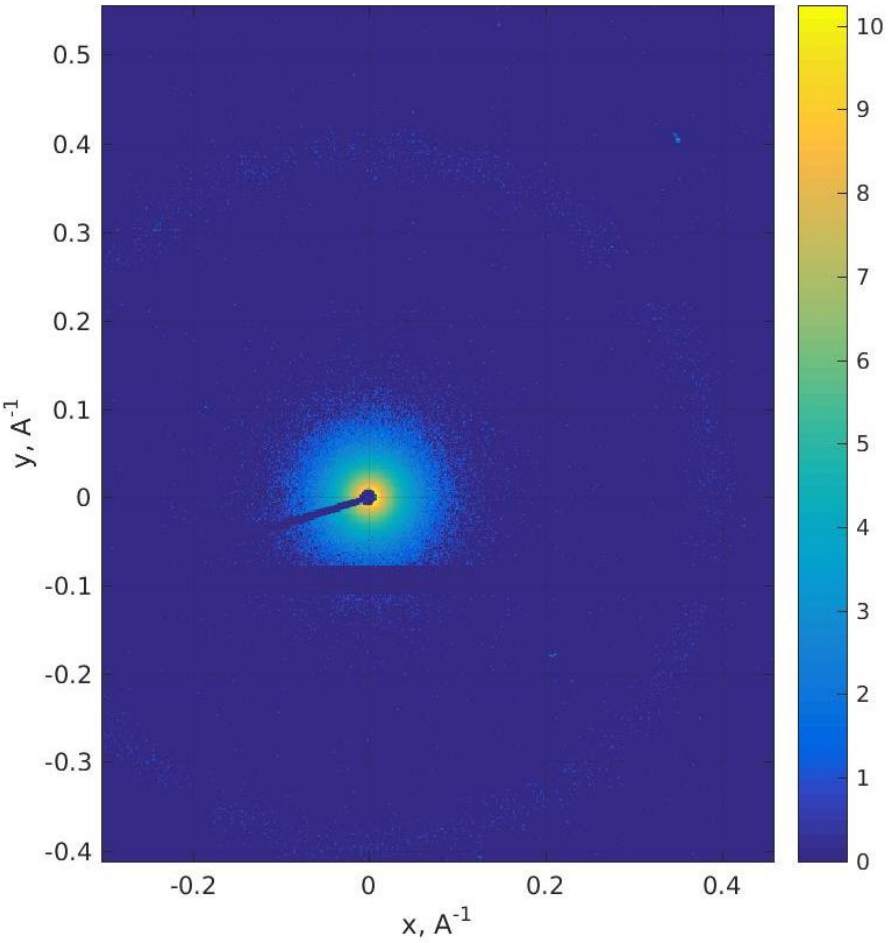

Fig. S11.

2D SAXS scattering plot of MDA at ~90 K illustrating the isotropic nature of the ice sample. The scattering intensity difference is shown according to the color legend on the right. X-rays along the beam axis are absorbed by a beam stopper before reaching the detector as can be seen from the dark central spot and line.

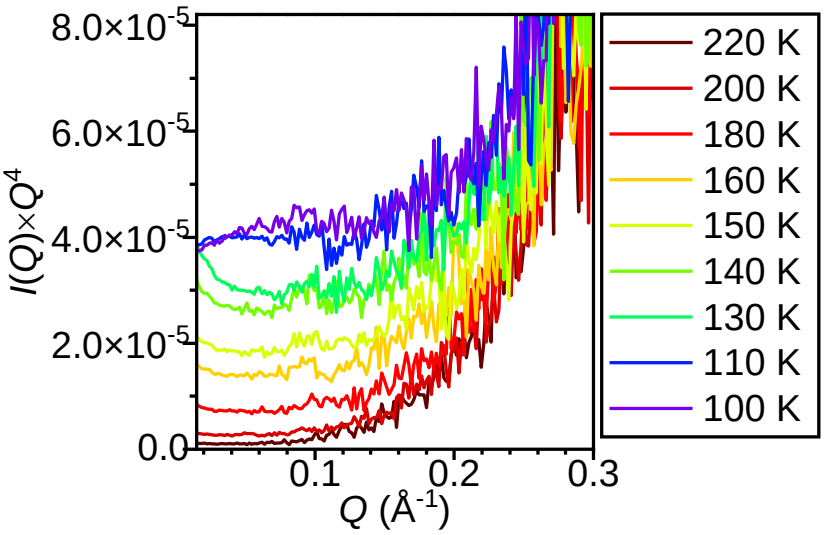

Fig. S12.

Test for Porod-law scattering of the SAXS data upon heating MDA from 100 to 220 K. The recorded scattering intensities are multiplied by Q^4 which means that Porod's law, $I(Q)=S\times Q^{-4}$, is followed where $I(Q)\times Q^4$ is horizontal.

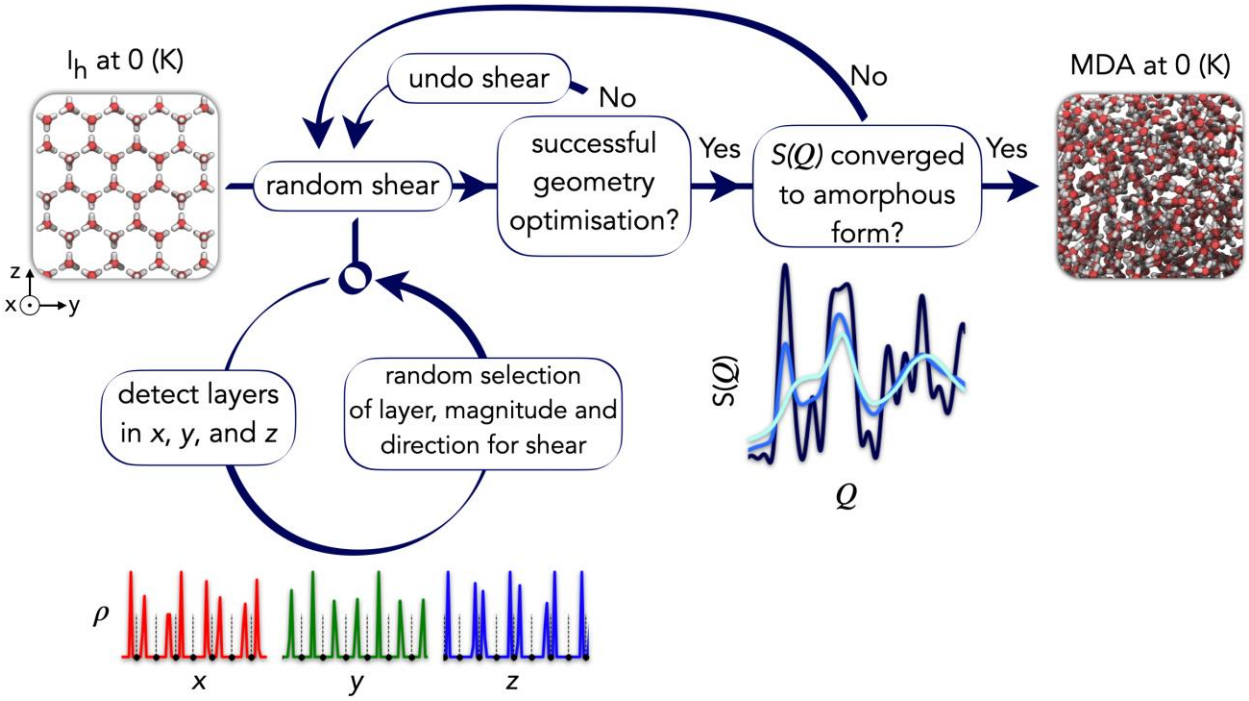

Fig. S13.

Schematic of the computational protocol for producing MDA from ice I*h*. The number density, ρ, was used to define possible layers to shear in *x*, *y* and *z*. Convergence of the structure factor, *S*(*Q*), was used to judge completion of the amorphization process.

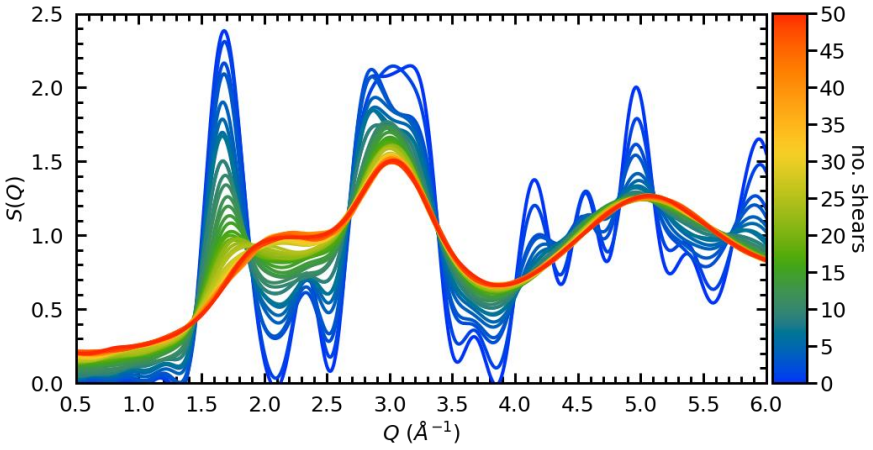

Fig. S14.

Evolution of the computational X-ray structure factor, *S*(*Q*), with the number of shears applied to the ice I*h* structure containing 2880 molecules at 0 K.

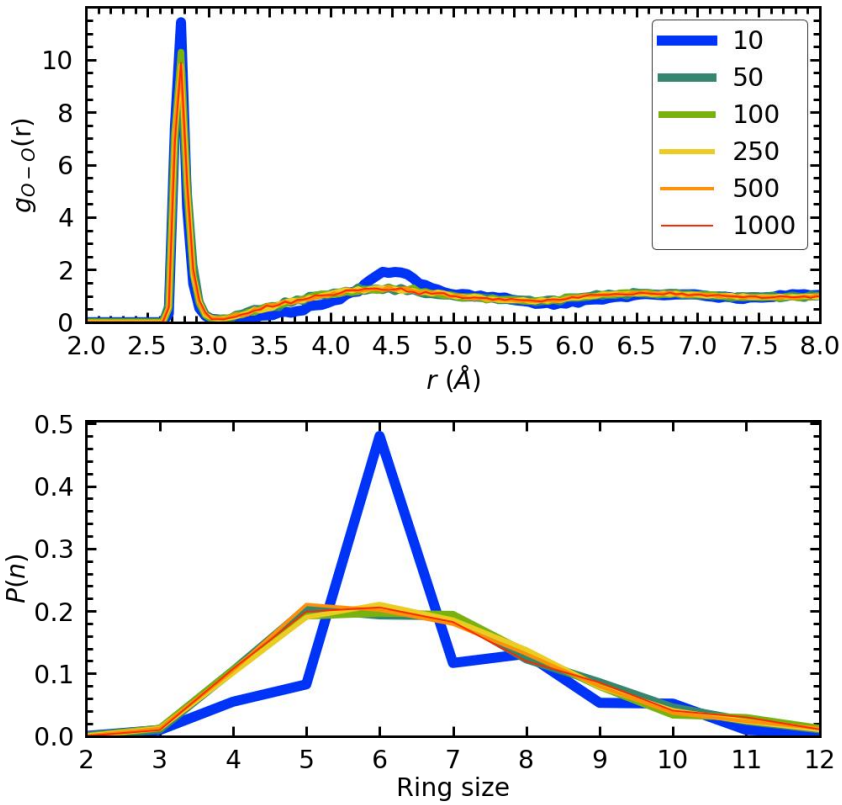

Fig. S15.

Evolution of the computational (top) oxygen-oxygen pair distribution function, $g_{o\text{-}o}(r)$, and (bottom) primitive ring-size distribution as a function of the shears applied to the ice I*h* structure with 2880 molecules at 0 K. The number of shears is indicated in the legend of the top panel.

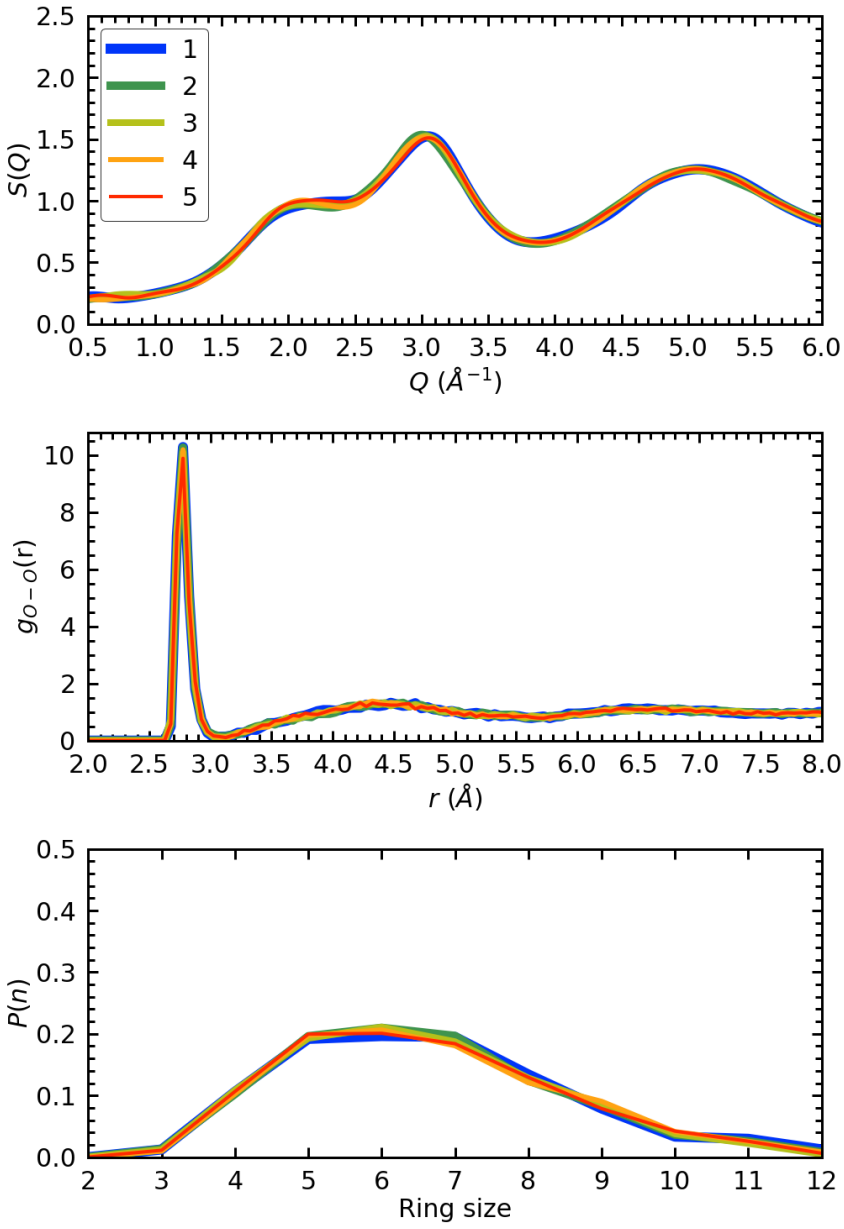

Fig. S16.

Computational structural properties for five independent shearing processes applied to the ice I*h* structure with 2880 molecules at 0 K. In each case, 100 shears have been applied. (top) X-ray structure factor, (middle) oxygen-oxygen pair distribution function and (bottom) primitive ring-size distribution. The colors corresponding to the individual shearing processes are shown in the legend of the top panel.

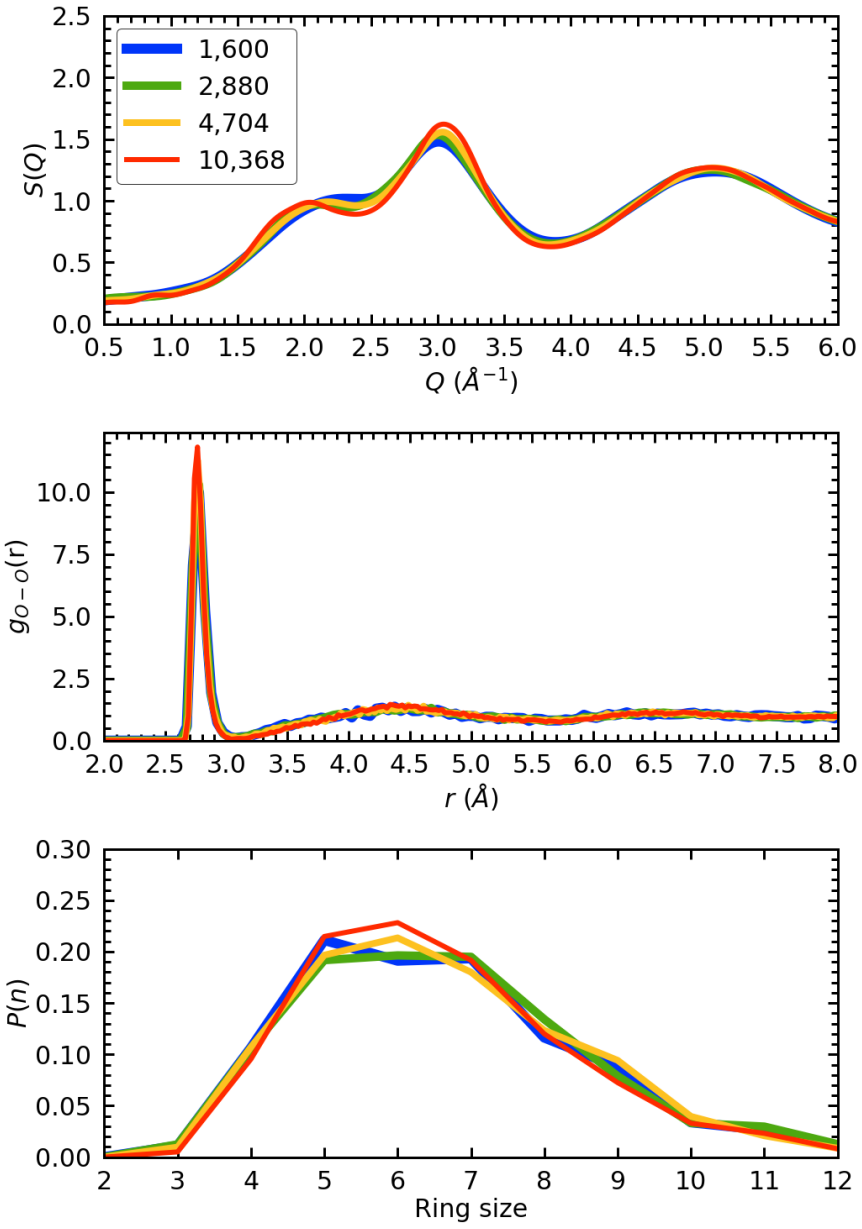

Fig. S17.

Computational structural properties of the MDA configurations at 0 K obtained from shearing differently sized ice I*h* structures containing 1660 (blue), 2880 (green), 4704 (yellow) and 10368 (red) water molecules. (top) X-ray structure factor, (middle) oxygen-oxygen pair distribution function, (bottom) primitive ring-size distribution.

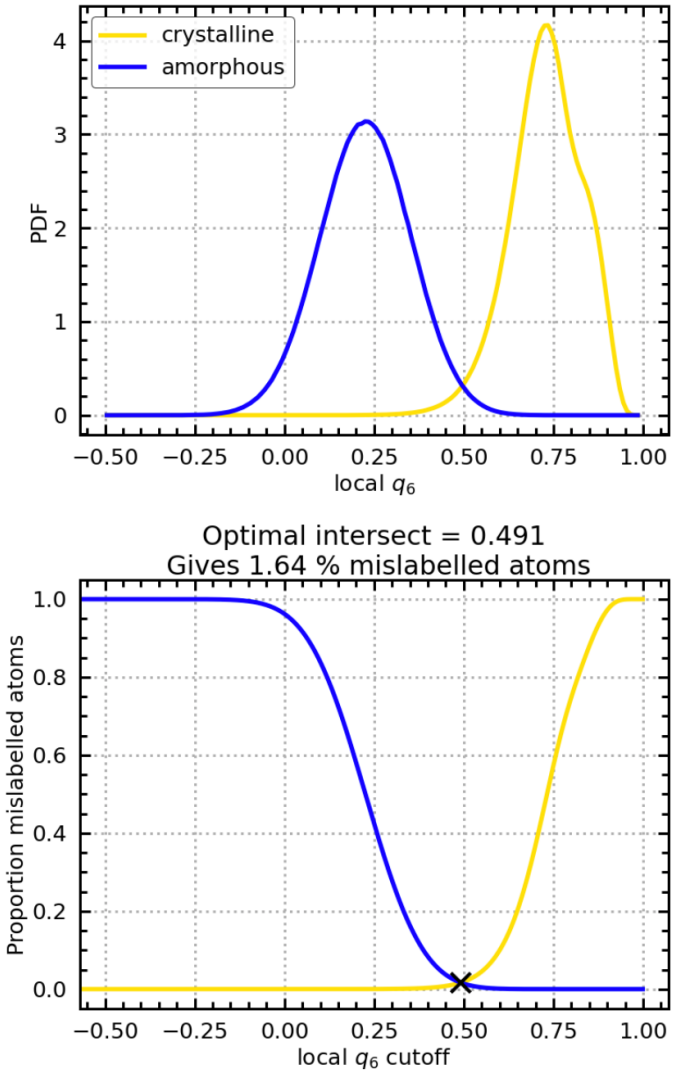

Fig. S18.

Procedure for identifying crystalline and amorphous local environments. (top) probability distribution functions (PDF) of local q_6 for water and ice at 250 K and 0 atm.(*64*) The PDF for ice comes from combining local q_6 from the bulk I*h* and I*c* simulations. (bottom) Proportion of mislabeled atoms for different choices of the local q_6 cutoff between crystalline and amorphous environments. The cutoff was taken where the probability of mislabeling a particle as crystalline when it is amorphous and vice versa is equal. The plugin for metadynamics (PLUMED2) was used to calculate local q_6.(*65*, *66*)

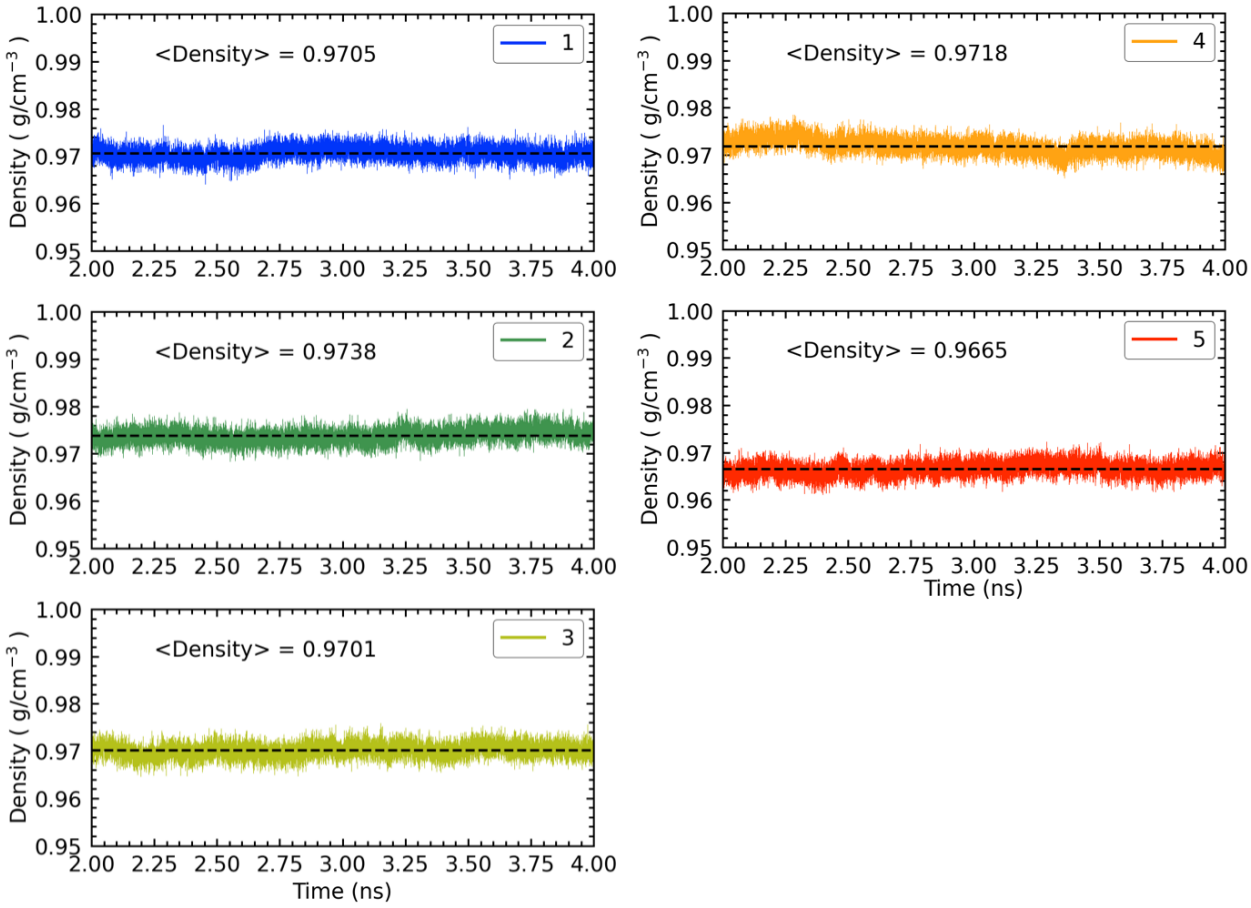

Fig. S19.

Computational determination of the density of MDA. Density as a function of time for simulations of five separate MDA configurations with data from the initial 2 ns equilibrations removed. Mean densities of the individual runs are illustrated by dashed horizontal lines.

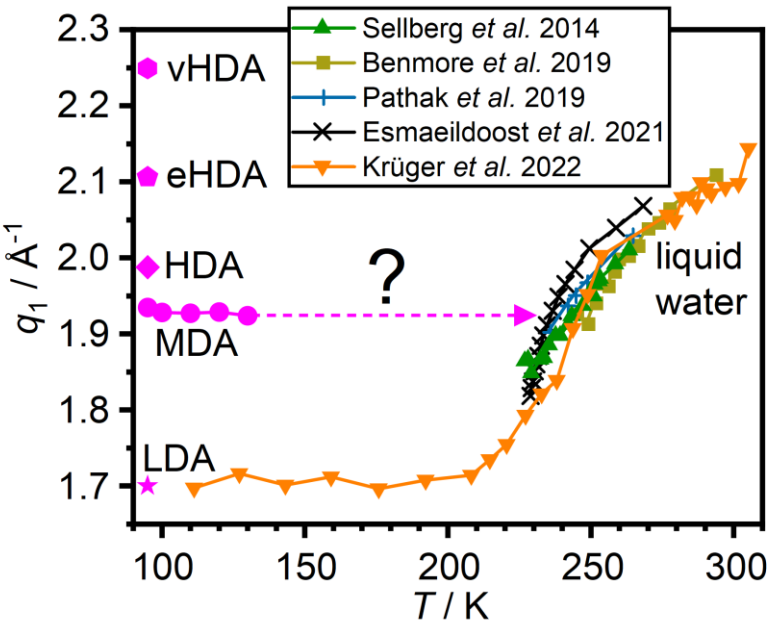

Fig. S20. Experimental positions of the first strong diffraction peaks of liquid water and the amorphous ices as a function of temperature.

The data points in magenta are from the X-ray diffraction measurements of the amorphous ices in this work (Fig. S4). The data of liquid water are taken from the X-ray diffraction measurements in refs (*67-70*) and electron diffraction in ref. (*71*). The question mark indicates a possible extrapolation from MDA towards supercooled water.

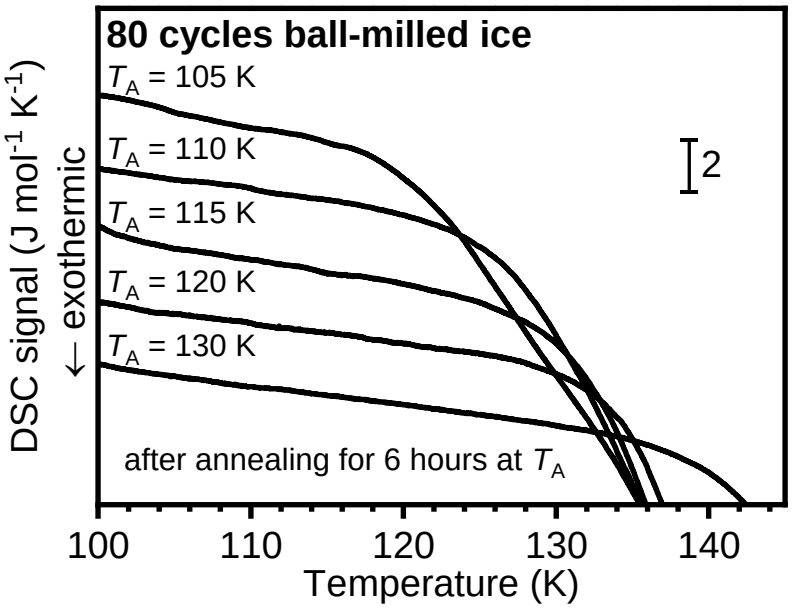

Fig. S21. Search for a glass transition of MDA.

DSC scans of MDA recorded at 10 K min^{-1} after annealing for 6 hours at the indicated temperatures. As shown for LDA,(*52*) annealing at temperatures below the crystallization temperature can yield endothermic steps in the heat capacity which is the calorimetric signature for a glass transition. No endothermic steps and therefore no glass transitions could be detected in any of the DSC scans of annealed MDA.

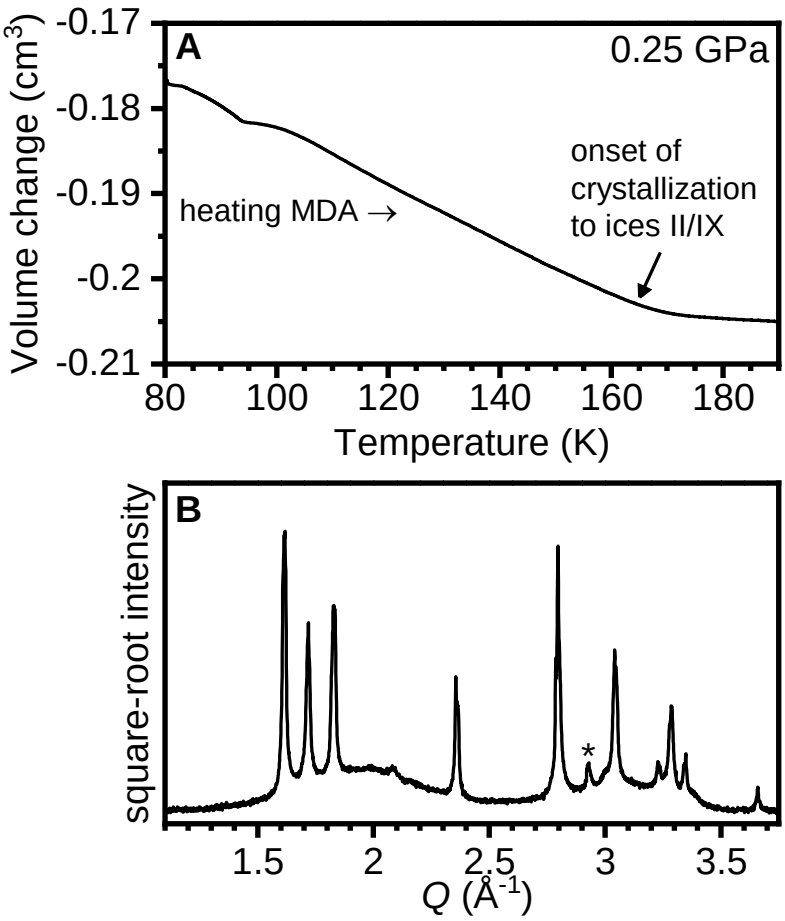

Fig. S22.

Heating MDA to the pressure / temperature conditions of formation of eHDA. (A) Volume changes recorded upon isobaric heating of MDA at 0.25 GPa. The onset of crystallization to ices II/IX is at ~165 K. (B) X-ray diffraction pattern of an MDA sample quenched after heating to 145 K at 0.25 GPa.

Movie S1.

Experimental procedure for making medium-density amorphous ice in the lab.

Movie S2.

Computational approach for making medium-density amorphous.

References

45. J. J. Shephard, B. Slater, P. Harvey, M. Hart, C. L. Bull, S. T. Bramwell, C. G. Salzmann, Doping-induced disappearance of ice II from water's phase diagram. *Nat. Phys.* **14**, 569-572 (2018).
46. A. B. Spierings, M. Schneider, R. Eggenberger, Comparison of density measurement techniques for additive manufactured metallic parts. *Rapid Prototyp. J.* **17**, 380-386 (2011).
47. K. Röttger, A. Endriss, J. Ihringer, S. Doyle, W. F. Kuhs, Lattice Constants and Thermal Expansion of H_2O and D_2O Ice Ih Between 10 and 265 K. *Acta Cryst.* **B50**, 644-648 (1994).
48. B. Kamb, Ice II: A Proton-Ordered Form of Ice. *Acta Cryst.* **17**, 1437-1449 (1964).
49. E. Mayer, R. Pletzer, Astrophysical Implications of Amorphous Ice - a Microporous Solid. *Nature* **319**, 298-301 (1986).
50. S. K. Talewar, S. O. Halukeerthi, R. Riedlaicher, J. J. Shephard, A. E. Clout, A. Rosu-Finsen, G. R. Williams, A. Langhoff, D. Johannsmann, C. G. Salzmann, Gaseous "Nanoprobes" for Detecting Gas-trapping Environments in Macroscopic Films of Vapor-deposited Amorphous Ice. *J. Chem. Phys.* **151**, 134505 (2019).
51. T. Loerting, K. Winkel, M. Seidl, M. Bauer, C. Mitterdorfer, P. H. Handle, C. G. Salzmann, E. Mayer, J. L. Finney, D. T. Bowron, How Many Amorphous Ices Are There? *Phys. Chem. Chem. Phys.* **13**, 8783-8794 (2011).
52. A. Hallbrucker, E. Mayer, Calorimetric Study of the Vitrified Liquid Water to Cubic Ice Phase Transition. *J. Phys. Chem.* **91**, 503-505 (1987).
53. O. Mishima, L. D. Calvert, E. Whalley, 'Melting Ice' I at 77 K and 10 kbar: A New Method of Making Amorphous Solids. *Nature* **310**, 393-395 (1984).
54. T. Loerting, C. Salzmann, I. Kohl, E. Mayer, A. Hallbrucker, A Second Distinct Structural "State" of High-density Amorphous Ice at 77 K and 1 bar. *Phys. Chem. Chem. Phys.* **3**, 5355-5357 (2001).
55. R. J. Nelmes, J. S. Loveday, T. Strässle, C. L. Bull, M. Guthrie, G. Hamel, S. Klotz, Annealed High-density Amorphous Ice Under Pressure. *Nat. Phys.* **2**, 414-418 (2006).
56. T. L. Malkin, B. J. Murray, C. G. Salzmann, V. Molinero, S. J. Pickering, T. F. Whale, Stacking Disorder in Ice I. *Phys. Chem. Chem. Phys.* **17**, 60-76 (2015).
57. C. G. Salzmann, B. J. Murray, J. J. Shephard, Extent of stacking disorder in diamond. *Diam. Relat. Mater.* **59**, 69-72 (2015).
58. J. L. F. Abascal, E. Sanz, R. García Fernández, C. Vega, A potential model for the study of ices and amorphous water: TIP4P/Ice. *J. Chem. Phys.* **122**, 234511 (2005).
59. M. Matsumoto, T. Yagasaki, H. Tanaka, Novel Algorithm to Generate Hydrogen-Disordered Ice Structures. *J. Chem. Inf. Model.* **61**, 2542-2546 (2021).
60. A. Hjorth Larsen, J. Jørgen Mortensen, J. Blomqvist, I. E. Castelli, R. Christensen, M. Dułak, J. Friis, M. N. Groves, B. Hammer, C. Hargus, E. D. Hermes, P. C. Jennings, P.

Bjerre Jensen, J. Kermode, J. R. Kitchin, E. Leonhard Kolsbjerg, J. Kubal, K. Kaasbjerg, S. Lysgaard, J. Bergmann Maronsson, T. Maxson, T. Olsen, L. Pastewka, A. Peterson, C. Rostgaard, J. Schiøtz, O. Schütt, M. Strange, K. S. Thygesen, T. Vegge, L. Vilhelmsen, M. Walter, Z. Zeng, K. W. Jacobsen, The atomic simulation environment—a Python library for working with atoms. *J. Phys.: Condens. Matter* **29**, 273002 (2017).

61. S. Plimpton, Fast Parallel Algorithms for Short-Range Molecular Dynamics. *J. Comp. Phys.* **117**, 1-19 (1995).
62. S. Le Roux, P. Jund, Ring statistics analysis of topological networks: New approach and application to amorphous GeS2 and SiO2 systems. *Comput. Mater. Sci.* **49**, 70-83 (2010).
63. D. Mariedahl, F. Perakis, A. Späh, H. Pathak, K. H. Kim, C. Benmore, A. Nilsson, K. Amann-Winkel, X-ray studies of the transformation from high- to low-density amorphous water. *Philos. Trans. Royal Soc. A* **377**, 20180164 (2019).
64. T. Li, D. Donadio, G. Russo, G. Galli, Homogeneous ice nucleation from supercooled water. *Phys. Chem. Chem. Phys.* **13**, 19807-19813 (2011).
65. M. Bonomi, D. Branduardi, G. Bussi, C. Camilloni, D. Provasi, P. Raiteri, D. Donadio, F. Marinelli, F. Pietrucci, R. A. Broglia, M. Parrinello, PLUMED: A portable plugin for free-energy calculations with molecular dynamics. *Comput. Phys. Commun.* **180**, 1961-1972 (2009).
66. G. A. Tribello, M. Bonomi, D. Branduardi, C. Camilloni, G. Bussi, PLUMED 2: New feathers for an old bird. *Comput. Phys. Commun.* **185**, 604-613 (2014).
67. J. A. Sellberg, C. Huang, T. A. McQueen, N. D. Loh, H. Laksmono, D. Schlesinger, R. G. Sierra, D. Nordlund, C. Y. Hampton, D. Starodub, D. P. DePonte, M. Beye, C. Chen, A. V. Martin, A. Barty, K. T. Wikfeldt, T. M. Weiss, C. Caronna, J. Feldkamp, L. B. Skinner, M. M. Seibert, M. Messerschmidt, G. J. Williams, S. Boutet, L. G. M. Pettersson, M. J. Bogan, A. Nilsson, Ultrafast X-ray probing ofwater structure below the homogeneous ice nucleation temperature. *Nature* **510**, 381-384 (2014).
68. H. Pathak, A. Späh, K. H. Kim, I. Tsironi, D. Mariedahl, M. Blanco, S. Huotari, V. Honkimäki, A. Nilsson, Intermediate range O–O correlations in supercooled water down to 235 K. *J. Chem. Phys.* **150**, 224506 (2019).
69. C. Benmore, L. C. Gallington, E. Soignard, Intermediate range order in supercooled water. *Mol. Phys.* **117**, 2470-2476 (2019).
70. N. Esmaeildoost, H. N. Pathak, A. Späh, T. J. Lane, K. H. Kim, C. Yang, K. Amann-Winkel, M. Ladd-Parada, F. Perakis, J. Koliyadu, A. R. Oggenfuss, P. Johnson, Y. Deng, S. Zerdane, R. Mankowsky, P. Beaud, L. Henrik, A. Nilsson, J. A. Sellberg, Anomalous temperature dependence of the experimental x-ray structure factor of supercooled water. *J. Chem. Phys.* **155**, 214501 (2021).
71. C. R. Krüger, N. J. Mowry, G. Bongiovanni, M. Drabbels, U. J. Lorenz, Electron Diffraction of Water in No Man's Land. arXiv:2211.04419 (2022).